J. Fluid Mech. (2002), *vol.* 454, *pp.* 419–442.
DOI: 10.1017/S0022112001007261 Printed in the United Kingdom

Stretching effects on the three-dimensional stability of vortices with axial flow

By IVAN DELBENDE[1], MAURICE ROSSI[2] AND STÉPHANE LE DIZÈS[3]

[1]LIMSI, CNRS–UPR 3251, BP 133, F-91403 Orsay Cedex, France
[2]LMM, Université Paris VI, 4 place Jussieu, F-75252 Paris Cedex 05, France
[3]IRPHE, CNRS–UMR 6594, 49 rue Joliot Curie, F-13384 Marseille Cedex 13, France

(Received 11 January 2001 and in revised form 23 July 2001)

The effect of stretching on the three-dimensional stability of a viscous unsteady vortex is addressed. The basic flow, which satisfies the Navier–Stokes equations, is a vortex with axial flow subjected to a time-dependent strain field oriented along its axis. The linear equations for the three-dimensional perturbations of the stretched vortex are first reduced by using successive changes of variables to equations which are almost identical to those of the unstretched vortex but with time-dependent parameters. These equations are then numerically solved in the particular case of the Batchelor vortex with a strain field which first compresses then stretches the vortex. Through this simulation, it is qualitatively demonstrated how the simultaneous action of stretching and azimuthal vorticity may destabilize a vortex. It is also argued that it provides a possible mechanism for the vortex bursts observed in turbulence experiments.

1. Introduction

On the one hand, axisymmetric vortices with axial flow are known to be subject to three-dimensional instabilities. On the other hand, stretching is known to modify both the vortex characteristic parameters and the evolution of the perturbations. In this work, general equations for the evolution of three-dimensional perturbations on a stretched vortex with axial flow are derived. The effect of stretching on instability is analysed, and a mechanism for the breakdown of vortices in turbulent flows is proposed.

Stretching is one of the important features that differentiate three-dimensional flows from two-dimensional flows as it prevents the local inviscid conservation of enstrophy. In three-dimensional flows, vorticity can be enhanced (resp. diminished) by stretching (resp. by compression) when oriented along a principal direction of strain. This effect is described well by the Lundgren (1982) transform which maps two-dimensional Navier–Stokes solutions to three-dimensional uniformly stretched (or compressed) solutions. In particular, this transform demonstrates that the main effect of an axial stretching/compression field is to modify the time and space characteristics (vorticity maximum and core radius) of the vortex. In a turbulent flow, one thus expects vorticity-filament characteristics to be continuously modified by the background stretching field generated by surrounding vortices. In this context, numerical studies have been recently performed where the stretching field acting on a straight vortex is non-uniform (Verzicco, Jiménez & Orlandi 1995), time-periodic

(Verzicco & Jiménez 1999), or generated by an array of vortex rings (Marshall 1997; Abid *et al.* 2002).

Stretching also appears to be important for the statistical properties of turbulence. Indeed, the only dynamical model which was successful in predicting the $k^{-5/3}$ energy spectrum of Kolmogorov turbulence was designed from uniformly stretched spiral vortices (Lundgren 1982; see also Pullin & Saffman 1998 for a review). However, despite its impressive success, the uniformly stretched vortex model used by Lundgren is too simple as vorticity is always aligned with the vortex axis and with a principal direction of strain.

This limitation has recently been overcome by Gibbon, Fokas & Doering (1999) who extended Lundgren's solutions to account for an axial flow component along the vortex axis. Their solutions are interesting because both axial and azimuthal vorticity are now present and because the stretching field is no longer uniform. These new features make these solutions very attractive for vortex filament models in turbulent flows. The presence of axial flow along the vortex axis, which appears to be ubiquitous in stretched vortices (see for instance Andreotti, Douady & Couder 1997 and Petitjeans *et al.* 1998) could in particular explain some dynamical behaviours of vortex filaments in turbulent flows such as bursts or vortex breakdowns. Indeed, the latter phenomenon, which is characterized by a localized blow-up of the vortex core and the appearance of a stagnation point has always been associated with axial flows. Although there is still a controversy about whether or not vortex instability is needed for vortex breakdown,† it is established that unstable modes do exist in vortices with axial flow, especially in the Batchelor vortex. This vortex was introduced by Batchelor (1964) in the context of an asymptotic description of trailing vortices. Both its axial vorticity and axial velocity have the same Gaussian profile. More generally it constitutes an exact solution of the Navier–Stokes equations if one takes into account the modification of the core radius due to viscous diffusion. This weak time-dependence effect has usually been neglected and the Batchelor vortex has been considered as a stationary solution on which normal modes exist. Temporal instability properties are given by Lessen, Singh & Paillet (1974), Lessen & Paillet (1974), Mayer & Powell (1992) and Ash & Khorrami (1995). These authors showed that for large Reynolds numbers and intermediate swirl numbers q ($0 < q < 1.5$), where q is defined as the ratio of azimuthal to axial velocity, the instability is dominated by inviscid negative helical modes. These modes become stable for swirl numbers larger than 1.5. The absolute/convective character of this instability was analysed by Olendraru *et al.* (1996, 1999) and Delbende, Chomaz & Huerre (1998).

In the present paper, we consider a Batchelor vortex subjected to a time-dependent stretching/compression field along its axis. Remarkably, Gibbon *et al.* (1999) showed that even subjected to a stretching field, the Batchelor vortex remains a Navier–Stokes solution provided its radius and swirl number follow particular time evolutions given in § 2. This general family of stretched vortices naturally contains Burgers' vortex as a particular case (constant stretching and infinite swirl number). Our goal is here to analyse the linear evolution of three-dimensional perturbations on such a time-evolving flow. More specifically, we address the issue of whether three-dimensional perturbations on the stretched vortex are related to those on the unstretched one.

So far, the effect of stretching on three-dimensional perturbations has been analysed

† Vortex breakdown, i.e. the appearance of a stagnation point, occurs in various geometries (boxes with rotating ends, cylinders with varying diameter) for which other theories exist (see Leibovich 1978, 1983 and Escudier 1988 for a review).

only in the context of vortices without axial flow. Rossi & Le Dizès (1997) showed that the three-dimensional temporal spectrum of steady stretched vortices (axisymmetric or not) only contains modes which are independent of the axial coordinate (stretching axis). The effect of stretching on the elliptical instability of a vortex was analysed by Le Dizès, Rossi & Moffatt (1996) for a uniform vorticity flow and by Eloy & Le Dizès (1999) for an elliptically deformed Gaussian vortex. In both instances, the authors showed that stretching tends to limit the growth of the unstable modes in time, and therefore to stabilize the vortex for a sufficiently strong stretching rate.

In the present paper, the same issue is addressed for the Batchelor-vortex instability. However, by contrast with asymptotic analyses of the elliptical instability, a direct numerical simulation is used here, whereby a time-varying stretching rate is considered. In this framework, the selection process of the most unstable perturbations from white noise initial conditions is considered.

The paper is organized as follows. In § 2, the results of Gibbon *et al.* (1999) are reviewed and the stretched Batchelor vortex solution, which is considered in the rest of the paper, is presented. In § 3, the equations governing the dynamics of linear three-dimensional perturbations to the stretched Batchelor vortex are derived. It is shown how they are related to those for the unstretched vortex via changes of variables and a quasi-static approximation. The numerical procedure used for the simulations is then presented in § 4: it is a velocity/vorticity pseudo-spectral method adapted to the current problem. Results are given and discussed in § 5.

2. The basic flow

Gibbon *et al.* (1999) recently obtained new exact solutions to the Navier–Stokes equations which extend the solutions previously used by Lundgren (1982). In the case of an axisymmetric flow, the velocity field of these solutions has, in polar coordinates (r, θ, z), the following form:

$$U_r^{\mathrm{tot}}(r,t) = -\frac{\gamma(t)}{2} r, \tag{2.1}$$

$$U_\theta^{\mathrm{tot}}(r,t) = U_\theta(r,t), \tag{2.2}$$

$$W^{\mathrm{tot}}(r,z,t) = \gamma(t) z + W(r,t), \tag{2.3}$$

which is a combination of an axisymmetric vortex of azimuthal velocity $U_\theta(r,t)$, an axial jet of velocity $W(r,t)$ and an unsteady linear stretching field of strain rate $\gamma(t)$. These solutions are more general than the Burgers vortex as vorticity is not necessarily aligned along with the vortex axis or with a principal direction of strain. Indeed, there are both an axial and an azimuthal component of vorticity, given by

$$\Omega_z^{\mathrm{tot}}(r,t) = \frac{1}{r}\frac{\partial (r U_\theta)}{\partial r}, \quad \Omega_\theta^{\mathrm{tot}}(r,t) = -\frac{\partial W}{\partial r}.$$

Gibbon *et al.* (1999) showed that the governing equations reduce to a system of three equations for Ω_z^{tot}, W and γ:

$$\frac{\mathrm{D}\Omega_z^{\mathrm{tot}}}{\mathrm{D}t} = \gamma \Omega_z^{\mathrm{tot}} + \nu \Delta \Omega_z^{\mathrm{tot}}, \tag{2.4}$$

$$\frac{\mathrm{D}W}{\mathrm{D}t} = -\gamma W + \nu \Delta W, \tag{2.5}$$

$$\frac{\mathrm{D}\gamma}{\mathrm{D}t} + \gamma^2 + \frac{\partial^2 P^{\mathrm{tot}}}{\partial z^2} = \nu \Delta \gamma, \tag{2.6}$$

where

$$\frac{\mathrm{D}}{\mathrm{D}t} \equiv \frac{\partial}{\partial t} - \frac{\gamma r}{2}\frac{\partial}{\partial r}.$$

In system (2.4)–(2.6), ν stands for the fluid kinematic viscosity and the second partial z-derivative of the pressure P^{tot} is assumed uniform. Here, we impose the strain rate $\gamma(t)$ and deduce the pressure from

$$P^{\mathrm{tot}}(r,t) = \int_0^r \frac{U_\theta^2(r',t)}{r'}\mathrm{d}r' + \left(\frac{\mathrm{d}\gamma}{\mathrm{d}t} - \frac{\gamma^2}{2}\right)\frac{r^2}{4} - \left(\frac{\mathrm{d}\gamma}{\mathrm{d}t} + \gamma^2\right)\frac{z^2}{2}. \tag{2.7}$$

Note that equations (2.4) and (2.5) demonstrate that axial vorticity is enhanced by stretching while axial velocity and azimuthal vorticity are reduced. The dynamical exchange between the different vorticity components makes these solutions richer than unidirectional vortices and probably better candidates for vortex filament models.

When stretching/compression terms are discarded, equations (2.4) and (2.5) reduce to radial diffusion equations which are known to possess a Gaussian kernel. Using time and space rescalings, Gibbon *et al.* (1999) have extended this property, finding the following self-similar solution of (2.4) and (2.5):

$$U_\theta(r,t) = \frac{\Gamma}{2\pi r}\left[1 - \exp\left(-\frac{r^2}{a^2}\right)\right], \tag{2.8}$$

$$W(r,t) = \frac{W_0}{s^2(a/a_0)^2}\exp\left(-\frac{r^2}{a^2}\right), \tag{2.9}$$

where $a(t)$ denotes the vortex core size, a_0 its initial value, Γ the constant vortex circulation, W_0 the initial centreline velocity, and $s(t)$ the dimensionless quantity

$$s(t) = \exp\left(\int_0^t \gamma(u)\mathrm{d}u\right). \tag{2.10}$$

The core size $a(t)$, which has been chosen identical for both axial and azimuthal velocity components, depends on the kinematic viscosity ν and the strain rate $\gamma(t)$ via

$$a^2(t) = \frac{a_0^2 + 4\nu\tau}{s}, \tag{2.11}$$

where

$$\tau = \int_0^t s(u)\mathrm{d}u \tag{2.12}$$

stands for a modified time which coincides with time t in the case of zero strain $\gamma = 0$.

At each time t, expressions (2.8) and (2.9) for U_θ and W characterize an instantaneous Batchelor vortex of radius $a(t)$ and swirl number $q(t)$, where

$$q(t) = \frac{\Gamma}{2\pi a_0^2 W_0}s^2 a$$

denotes the ratio of the characteristic azimuthal velocity $\Gamma/(2\pi a)$ to the centreline axial velocity $W_0 a_0^2/(s^2 a^2)$.

The present paper is aimed at investigating the three-dimensional stability properties of solution (2.1)–(2.3) with the Batchelor profiles (2.8) and (2.9). The same analysis is naturally possible with other profiles but would require the consideration of varying profiles which always tend towards the Batchelor profile through viscous diffusion.

Hence the choice of the Batchelor profile is natural. Moreover, the stability properties of the unstretched Batchelor vortex are well-known, which allows a direct comparison between stretched and unstretched cases.

As mentioned above, the time-evolution of the characteristic parameters of the Batchelor vortex depends on the way the strain rate varies. One could imagine that in a turbulent environment this variation would be coupled to the dynamics of distant vortices (via the pressure term in equation (2.6)). Such an explicit coupling is not considered here, but will be modelled by a particular variation of the strain rate. Moreover, only perturbations which are localized in the vortex core are considered. In the numerical part § 5.2 of the present study, the basic flow (2.1)–(2.3) evolves in time as follows. For $0 \leqslant t < t_\star$, the vortex is compressed with a constant negative strain rate $\gamma = -\gamma_0 < 0$, so that

$$s(t) = \exp(-\gamma_0 t), \tag{2.13}$$

$$\tau(t) = \frac{1 - \exp(-\gamma_0 t)}{\gamma_0}, \tag{2.14}$$

$$a^2(t) = \left(a_0^2 + \frac{4\nu}{\gamma_0}\right)\exp(\gamma_0 t) - \frac{4\nu}{\gamma_0}. \tag{2.15}$$

When time t varies from 0 to $t_\star$, the modified time τ and the characteristic radius $a(t)$ increase. By definition, τ varies from 0 to $\tau_\star$ such that $\tau_\star \gamma_0 = 1 - \exp(-\gamma_0 t_\star)$; in particular, if $t_\star = \infty$, $\tau_\star = 1/\gamma_0$. If $t_\star$ is large enough, there exists a time t_q after which the swirl number $q(t)$ decreases, i.e. the jet component of the flow increases with respect to the swirling component. The value of t_q depends on the relative size of a_0 with respect to $(\nu/\gamma_0)^{1/2}$.

For $t \geqslant t_\star$, the vortex is stretched with the opposite strain rate $\gamma = \gamma_0 > 0$:

$$s(t) = s(t_\star)\exp[\gamma_0(t - t_\star)], \tag{2.16}$$

$$\tau(t) = \tau(t_\star) + \frac{s(t) - s(t_\star)}{\gamma_0} = \tau_\star + s(t_\star)\frac{\exp[\gamma_0(t - t_\star)] - 1}{\gamma_0}, \tag{2.17}$$

$$a^2(t) = \left[a^2(t_\star) - \frac{4\nu}{\gamma_0}\right]\exp\left[-\gamma_0(t - t_\star)\right] + \frac{4\nu}{\gamma_0}. \tag{2.18}$$

Time t varies from $t_\star$ to $+\infty$ when variable τ increases from $\tau_\star$ to $+\infty$. The characteristic radius $a(t)$ tends towards a finite value $2(\nu/\gamma_0)^{1/2}$ while the swirl number $q(t)$ increases to $+\infty$. In this case, the jet component always decreases with respect to the swirling component. Asymptotically one recovers a stationary stretched vortex aligned with the z-axis and subjected to a global strain field, i.e. the well-known Burgers vortex governed by the balance between stretching and viscous diffusion.

Note that, from a mathematical point of view, quantity $\gamma(t)$ might *a priori* follow any time dependence, so that steady or time-periodic† functions could be used instead of (2.13)–(2.18). However, we expect quantity $\gamma(t)$, which models the action of large structures on the vortex, to fluctuate with a characteristic time larger than the turnover time. Our choice has been guided by simplicity: the selected time dependence is the simplest fluctuation containing a single stretching and compression phase.

† A time-periodic fluctuation is of interest if its period becomes of the same order as the turnover time.

3. Linear three-dimensional perturbations: governing equations

In this section, the three-dimensional stability equations of the stretched vortex with basic flow velocity $\boldsymbol{U}^{\mathrm{tot}}(t)$ are considered. It is shown how the evolution of three-dimensional perturbations are connected to those in an unstretched vortex.

The dynamics of infinitesimal pressure p and velocity $\boldsymbol{u}$ perturbations is governed by the linear system

$$\partial_t \boldsymbol{u} + (\boldsymbol{U}^{\mathrm{tot}}(t)\cdot\nabla)\boldsymbol{u} + (\boldsymbol{u}\cdot\nabla)\boldsymbol{U}^{\mathrm{tot}}(t) = -\nabla p + \nu\Delta\boldsymbol{u}, \tag{3.1}$$

$$\nabla\cdot\boldsymbol{u} = 0, \tag{3.2}$$

which is inhomogeneous with respect to time t and spatial coordinates r and z. In polar coordinates, the above equations for perturbations $\boldsymbol{u} = (u, v, w)$ and p are

$$\frac{\mathrm{D}u}{\mathrm{D}t} - \frac{\gamma(t)}{2}u - 2\frac{U_\theta(r,t)}{r}v = -\frac{1}{\rho}\frac{\partial p}{\partial r} + \nu(\Delta\boldsymbol{u})_r, \tag{3.3}$$

$$\frac{\mathrm{D}v}{\mathrm{D}t} - \frac{\gamma(t)}{2}v + \left(\frac{\partial U_\theta(r,t)}{\partial r} + \frac{U_\theta(r,t)}{r}\right)u = -\frac{1}{\rho r}\frac{\partial p}{\partial\theta} + \nu(\Delta\boldsymbol{u})_\theta, \tag{3.4}$$

$$\frac{\mathrm{D}w}{\mathrm{D}t} + \gamma(t)w + \frac{\partial W}{\partial r}u = -\frac{1}{\rho}\frac{\partial p}{\partial z} + \nu(\Delta\boldsymbol{u})_z, \tag{3.5}$$

$$\frac{\partial u}{\partial r} + \frac{u}{r} + \frac{1}{r}\frac{\partial v}{\partial\theta} + \frac{\partial w}{\partial z} = 0, \tag{3.6}$$

where $\nu(\Delta\boldsymbol{u})_r$, $\nu(\Delta\boldsymbol{u})_\theta$ and $\nu(\Delta\boldsymbol{u})_z$ denote the classical polar components of the viscous term and $\mathrm{D}/\mathrm{D}t$ stands for the convective derivative relative to the basic state:

$$\frac{\mathrm{D}}{\mathrm{D}t} \equiv \frac{\partial}{\partial t} - \frac{\gamma(t)r}{2}\frac{\partial}{\partial r} + \frac{U_\theta(r,t)}{r}\frac{\partial}{\partial\theta} + (W(r,t) + \gamma(t)z)\frac{\partial}{\partial z}. \tag{3.7}$$

This stability problem cannot be handled by a standard Fourier transform technique because of the explicit space and time dependences. However, the present section provides a connection between equations (3.1)–(3.7) and the linear equations governing the dynamics of infinitesimal disturbances in an axisymmetric time-dependent unstretched basic flow. This is reminiscent of the Lundgren transformation

$$t \longrightarrow \tau = \int_0^t s(u)\mathrm{d}u, \tag{3.8}$$

$$r \longrightarrow \bar{r} = \sqrt{s(t)}r, \tag{3.9}$$

$$\theta \longrightarrow \theta, \tag{3.10}$$

which precisely relates the basic flow $\boldsymbol{U}^{\mathrm{tot}}(t)$ to the Navier–Stokes solution formed by the diffusing unstretched Batchelor vortex $(0, U_\theta^{2\mathrm{D}}(\bar{r},\tau), W^{2\mathrm{D}}(\bar{r},\tau))$, where

$$U_\theta^{2\mathrm{D}}(\bar{r},\tau) = \frac{U_\theta(\bar{r}/\sqrt{s(t)},t)}{\sqrt{s(t)}} = \frac{\Gamma}{2\pi\bar{r}}\left[1 - \exp\left(-\frac{\bar{r}^2}{a_0^2 + 4\nu\tau}\right)\right] \tag{3.11}$$

$$W^{2\mathrm{D}}(\bar{r},\tau) = s(t)W(\bar{r}/\sqrt{s(t)},t) = \frac{W_0 a_0^2}{a_0^2 + 4\nu\tau}\exp\left(-\frac{\bar{r}^2}{a_0^2 + 4\nu\tau}\right). \tag{3.12}$$

An appropriate change of variables is now applied on the stability equations (3.1)–(3.7) which eliminates the terms relative to stretching as well as the explicit z-dependence.

To this end, in addition to Lundgren's transformation (3.8)–(3.10), a change of variable for z

$$z \longrightarrow \bar{z} = \frac{z}{s(t)} \tag{3.13}$$

is performed. This transformation, which is often written in terms of a time-dependent wavenumber, is commonly used in the context of inertial waves (see Craik & Criminale 1986) or rapid distortion theory (Batchelor & Proudman 1954; Cambon & Scott 1999).

Such changes of variable neither modify the partial derivatives with respect to θ nor affect the elementary volume. Moreover the following relations hold:

$$\frac{\partial}{\partial t} = S(\tau)\frac{\partial}{\partial \tau} + \frac{\mathrm{d}S}{\mathrm{d}\tau}\frac{\bar{r}}{2}\frac{\partial}{\partial \bar{r}} - \frac{\mathrm{d}S}{\mathrm{d}\tau}\bar{z}\frac{\partial}{\partial \bar{z}} \tag{3.14}$$

and

$$\frac{\partial}{\partial r} = \sqrt{S(\tau)}\frac{\partial}{\partial \bar{r}}, \quad \frac{\partial}{\partial z} = \frac{1}{S(\tau)}\frac{\partial}{\partial \bar{z}}, \tag{3.15}$$

where the function $S(\tau) \equiv s(t)$ satisfies

$$\gamma(t) = \frac{\mathrm{d}S}{\mathrm{d}\tau} = \frac{1}{s}\frac{\mathrm{d}s}{\mathrm{d}t}. \tag{3.16}$$

Transformation (3.8)–(3.9) (resp. (3.13)) eliminates the term $-\frac{1}{2}\gamma r\partial_r$ (resp. $\gamma z\partial_z$) in the convective derivative, which then becomes

$$\frac{\mathrm{D}}{\mathrm{D}t} = S(\tau)\frac{\bar{\mathrm{D}}}{\bar{\mathrm{D}}\tau}, \tag{3.17}$$

where

$$\frac{\bar{\mathrm{D}}}{\bar{\mathrm{D}}\tau} \equiv \frac{\partial}{\partial \tau} + \frac{U_\theta^{2\mathrm{D}}(\bar{r},\tau)}{\bar{r}}\frac{\partial}{\partial \theta} + \frac{W^{2\mathrm{D}}(\bar{r},\tau)}{S^3(\tau)}\frac{\partial}{\partial \bar{z}}. \tag{3.18}$$

It is readily seen that stretching has been explicitly eliminated in (3.18).

In accordance with equations (3.11)–(3.12), the following transformations are introduced to preserve the ratio between perturbations and basic state:

$$\bar{u} = \frac{u}{\sqrt{S}}, \quad \bar{v} = \frac{v}{\sqrt{S}}, \quad \bar{w} = Sw, \quad \bar{p} = \frac{p}{S}. \tag{3.19}$$

This procedure removes the amplification factor due to external strain which affects perturbation amplitudes. The complete linear system then becomes

$$\frac{\bar{\mathrm{D}}\bar{u}}{\bar{\mathrm{D}}\tau} - 2\frac{U_\theta^{2\mathrm{D}}}{\bar{r}}\bar{v} = -\frac{1}{\rho}\frac{\partial \bar{p}}{\partial \bar{r}} + \nu\left[(\Delta^{2\mathrm{D}}\bar{\boldsymbol{u}})_{\bar{r}} + \frac{1}{S^3}\frac{\partial^2 \bar{u}}{\partial \bar{z}^2}\right], \tag{3.20}$$

$$\frac{\bar{\mathrm{D}}\bar{v}}{\bar{\mathrm{D}}\tau} + \left(\frac{\partial U_\theta^{2\mathrm{D}}}{\partial \bar{r}} + \frac{U_\theta^{2\mathrm{D}}}{\bar{r}}\right)\bar{u} = -\frac{1}{\rho\bar{r}}\frac{\partial \bar{p}}{\partial \theta} + \nu\left[(\Delta^{2\mathrm{D}}\bar{\boldsymbol{u}})_{\theta} + \frac{1}{S^3}\frac{\partial^2 \bar{v}}{\partial \bar{z}^2}\right], \tag{3.21}$$

$$\frac{\bar{\mathrm{D}}\bar{w}}{\bar{\mathrm{D}}\tau} + \frac{\partial W^{2\mathrm{D}}}{\partial \bar{r}}\bar{u} = -\frac{1}{\rho}\frac{\partial \bar{p}}{\partial \bar{z}} + \nu\left[(\Delta^{2\mathrm{D}}\bar{\boldsymbol{u}})_{\bar{z}} + \frac{1}{S^3}\frac{\partial^2 \bar{w}}{\partial \bar{z}^2}\right], \tag{3.22}$$

$$\frac{\partial \bar{u}}{\partial \bar{r}} + \frac{\bar{u}}{\bar{r}} + \frac{1}{\bar{r}}\frac{\partial \bar{v}}{\partial \theta} + \frac{1}{S^3}\frac{\partial \bar{w}}{\partial \bar{z}} = 0. \tag{3.23}$$

Quantities $(\Delta^{2D}\bar{\boldsymbol{u}})_{\bar{r}}$, $(\Delta^{2D}\bar{\boldsymbol{u}})_{\theta}$ and $(\Delta^{2D}\bar{\boldsymbol{u}})_{\bar{z}}$ denote the components of the viscous Laplacian term in which the derivatives with respect to $\bar{z}$ are omitted:

$$(\Delta^{2D}\bar{\boldsymbol{u}})_{\bar{r}} = \frac{\partial}{\partial \bar{r}}\left[\frac{1}{\bar{r}}\frac{\partial(\bar{r}\bar{u})}{\partial \bar{r}}\right] + \frac{1}{\bar{r}^2}\frac{\partial^2 \bar{u}}{\partial \theta^2} - \frac{2}{\bar{r}^2}\frac{\partial \bar{v}}{\partial \theta}, \tag{3.24}$$

$$(\Delta^{2D}\bar{\boldsymbol{u}})_{\theta} = \frac{\partial}{\partial \bar{r}}\left[\frac{1}{\bar{r}}\frac{\partial(\bar{r}\bar{v})}{\partial \bar{r}}\right] + \frac{1}{\bar{r}^2}\frac{\partial^2 \bar{v}}{\partial \theta^2} + \frac{2}{\bar{r}^2}\frac{\partial \bar{u}}{\partial \theta}, \tag{3.25}$$

$$(\Delta^{2D}\bar{\boldsymbol{u}})_{\bar{z}} = \frac{1}{\bar{r}}\frac{\partial}{\partial \bar{r}}\left[\bar{r}\frac{\partial \bar{w}}{\partial \bar{r}}\right] + \frac{1}{\bar{r}^2}\frac{\partial^2 \bar{w}}{\partial \theta^2}. \tag{3.26}$$

This transformation thus shows that the two-dimensional stability ($\partial/\partial\bar{z} \equiv 0$) of a stretched vortex (2.1)–(2.3) is directly related to the two-dimensional stability problem for its unstretched and diffusing counterpart $(0, U_\theta^{2D}(\bar{r},\tau), W^{2D}(\bar{r},\tau))$, as already implied by Gibbon *et al.* (1999). For the general three-dimensional stability problem, the above system is quite close to the three-dimensional stability of the unstretched basic flow state $(0, U_\theta^{2D}(\bar{r},\tau), W^{2D}(\bar{r},\tau))$. It differs only through the presence of $1/S^3$ terms associated with $\bar{z}$-derivatives. In particular, equation (3.23) expresses the fluid incompressibility via a modified divergence-free condition. In system (3.20)–(3.23), the explicit time dependence originates (*a*) in the viscous diffusion acting on the unstretched basic Batchelor vortex, and (*b*) in the $1/S^3$ factors. A quasi-static approximation might help to understand the dynamics of perturbations, a feature that will be exploited in §5. Near a time τ_1, viscous diffusion is neglected in the basic state, i.e. the core size a is taken to be constant and equal to $a_1 = (a_0^2 + 4\nu\tau_1)^{1/2}$. Locally in time, this characteristic length scale a_1 provides a characteristic velocity scale $\Gamma/(2\pi a_1)$ and time scale $2\pi a_1^2/\Gamma$. Let us now assume that the non-dimensional strain rate $2\pi\gamma a_1^2/\Gamma$ is small. Such an hypothesis is generally made in turbulence studies where stretching due to large scales, typically of magnitude γa_1, is small with respect to the velocity in the vortex $\Gamma/(2\pi a_1)$. As a result, $S(\tau)$ is slowly evolving in time (see (3.16)), although it might be of order one. A quasi-static approximation is thus fully justified: near time τ_1, the parameter S is frozen, in the above equations, to its value $S_1 = S(\tau_1)$. Let $\Gamma/(2\pi a_1)$ be employed as a scale for velocity components $\bar{u}$ and $\bar{v}$, $\Gamma S_1^{3/2}/(2\pi a_1)$ as a scale for velocity component $\bar{w}$, $\rho[\Gamma/(2\pi a_1)]^2$ as a scale for pressure p, a_1 as length scale for $\bar{r}$, $a_1 S_1^{-3/2}$ as length scale for $\bar{z}$, and $2\pi a_1^2/\Gamma$ as time scale. Written in dimensionless form, the quasi-static equations are identical to the equations governing the linear perturbations of an unstretched Batchelor vortex with azimuthal and axial velocity respectively given by

$$U_\theta(\bar{r}) = \frac{1 - \exp(-\bar{r}^2)}{\bar{r}}, \tag{3.27}$$

$$W(\bar{r}) = \frac{1}{q}\exp(-\bar{r}^2), \tag{3.28}$$

with swirl and Reynolds numbers

$$q = \frac{S_1^{3/2}\Gamma a_1}{2\pi W_0 a_0^2}, \quad Re_\Gamma = \frac{\Gamma}{2\pi\nu}.$$

In this quasi-static approximation, the linear stability characteristics are thus directly connected to those of an unstretched Batchelor vortex. In particular, the swirl number q indicates whether we enter the region of the equivalent swirling jet instability.

4. Numerical formulation

For numerical purposes, the perturbation equations (3.20)–(3.23) are put in dimensionless form using the initial axial velocity W_0 as the velocity scale, the initial core size a_0 as the spatial scale, a_0/W_0 as time scale for t or τ and ρW_0^2 as the pressure scale:

$$\frac{\bar{\mathrm{D}}\bar{u}}{\bar{\mathrm{D}}\tau} - 2\frac{U_\theta^{2\mathrm{D}}}{\bar{r}}\bar{v} = -\frac{\partial\bar{p}}{\partial\bar{r}} + \frac{1}{Re}\left[(\Delta^{2\mathrm{D}}\bar{\boldsymbol{u}})_{\bar{r}} + \frac{1}{S^3}\frac{\partial^2\bar{u}}{\partial\bar{z}^2}\right], \tag{4.1}$$

$$\frac{\bar{\mathrm{D}}\bar{v}}{\bar{\mathrm{D}}\tau} + \left(\frac{\partial U_\theta^{2\mathrm{D}}}{\partial\bar{r}} + \frac{U_\theta^{2\mathrm{D}}}{\bar{r}}\right)\bar{u} = -\frac{1}{\bar{r}}\frac{\partial\bar{p}}{\partial\theta} + \frac{1}{Re}\left[(\Delta^{2\mathrm{D}}\bar{\boldsymbol{u}})_\theta + \frac{1}{S^3}\frac{\partial^2\bar{v}}{\partial\bar{z}^2}\right], \tag{4.2}$$

$$\frac{\bar{\mathrm{D}}\bar{w}}{\bar{\mathrm{D}}\tau} + \frac{\partial W^{2\mathrm{D}}}{\partial\bar{r}}\bar{u} = -\frac{\partial\bar{p}}{\partial\bar{z}} + \frac{1}{Re}\left[(\Delta^{2\mathrm{D}}\bar{\boldsymbol{u}})_{\bar{z}} + \frac{1}{S^3}\frac{\partial^2\bar{w}}{\partial\bar{z}^2}\right], \tag{4.3}$$

$$\frac{\partial\bar{u}}{\partial\bar{r}} + \frac{\bar{u}}{\bar{r}} + \frac{1}{\bar{r}}\frac{\partial\bar{v}}{\partial\theta} + \frac{1}{S^3}\frac{\partial\bar{w}}{\partial\bar{z}} = 0, \tag{4.4}$$

where the convective derivative $\bar{\mathrm{D}}/\bar{\mathrm{D}}\tau$ is

$$\frac{\bar{\mathrm{D}}}{\bar{\mathrm{D}}\tau} = \left[\frac{\partial}{\partial\tau} + \frac{U_\theta^{2\mathrm{D}}(\bar{r},\tau)}{\bar{r}}\frac{\partial}{\partial\theta} + \frac{W^{\mathrm{D}}(\bar{r},\tau)}{S^3(\tau)}\frac{\partial}{\partial\bar{z}}\right]. \tag{4.5}$$

Three dimensionless parameters are of importance here, namely the Reynolds number Re, the initial swirl number q_0 and the dimensionless strain rate $\tilde{\gamma}(\tau)$:

$$q_0 = \frac{\Gamma}{2\pi a_0 W_0}, \quad Re = \frac{W_0 a_0}{\nu} = \frac{Re_\Gamma}{q_0}, \quad \tilde{\gamma}(\tau) = \frac{\gamma a_0}{W_0}. \tag{4.6}$$

When the strain rate $\tilde{\gamma}$ is constant during a time interval $[\tau_\star, \tau]$, recall that the dimensionless parameter S satisfies $S(\tau) = S(\tau_\star) + \tilde{\gamma}(\tau - \tau_\star)$.

The basic flow in (4.1)–(4.4) evolves in time according to

$$U_\theta^{2\mathrm{D}}(\bar{r},\tau) = \frac{q_0}{\bar{r}}\left[1 - \exp\left(-\frac{\bar{r}^2}{1+4\tau/Re}\right)\right], \tag{4.7}$$

$$W^{2\mathrm{D}}(\bar{r},\tau) = \frac{1}{1+4\tau/Re}\exp\left(-\frac{\bar{r}^2}{1+4\tau/Re}\right). \tag{4.8}$$

In the subsequent analyses, we focus on a period of time much smaller than the one in which viscous diffusion acts on the basic flow, i.e. we assume that $4\tau/Re \ll 1$ in (4.7)–(4.8). Indeed for high Reynolds numbers $Re \gg 1$, such a time may be large with respect to the time in which instability takes place. Note that, within this approximation, $a_1 = a_0$ and the instantaneous swirl number is

$$q(\tau) = \frac{S^{3/2}\Gamma}{2\pi a_0 W_0} = S^{3/2} q_0 \ . \tag{4.9}$$

In the remaining part of this section, bars are omitted in order to simplify the notation. Equations (4.1)–(4.3) may then be recast as follows:

$$\partial_\tau\boldsymbol{u} + (\boldsymbol{U}^{2\mathrm{D}}\cdot\nabla)\boldsymbol{u} + (\boldsymbol{u}\cdot\nabla)\boldsymbol{U}^{2\mathrm{D}} = \left(1 - \frac{1}{S^3}\right)W^{2\mathrm{D}}\partial_z\boldsymbol{u} - \nabla p + \frac{1}{Re}\left(\Delta^{2\mathrm{D}}\boldsymbol{u} + \frac{1}{S^3}\frac{\partial^2\boldsymbol{u}}{\partial z^2}\right), \tag{4.10}$$

where the field $\boldsymbol{U}^{2D}$ is now stationary, and is given in polar coordinates by

$$\boldsymbol{U}^{2D}(r) = (0, U_\theta^{2D}(r), W^{2D}(r)). \tag{4.11}$$

The numerical code used in the present paper is adapted from Vincent & Meneguzzi (1991). It is written using the velocity/vorticity formulation pertaining to formula (4.10):

$$\partial_\tau \boldsymbol{u} = \boldsymbol{U}^{2D} \times \boldsymbol{\omega} + \boldsymbol{u} \times \boldsymbol{\Omega}^{2D} + \left(1 - \frac{1}{S^3}\right) W^{2D} \partial_z \boldsymbol{u} \\ -\nabla(p + \boldsymbol{U}^{2D} \cdot \boldsymbol{u}) + \frac{1}{Re}\left(\Delta^{2D}\boldsymbol{u} + \frac{1}{S^3}\frac{\partial^2 \boldsymbol{u}}{\partial z^2}\right), \tag{4.12}$$

where $\boldsymbol{\Omega}^{2D} = \nabla \times \boldsymbol{U}^{2D}$ and $\boldsymbol{\omega} = \nabla \times \boldsymbol{u}$. So far, the incompressibility condition (4.4) has not been used. Equation (4.12) may be expressed in the spectral domain relative to the three Cartesian directions (x, y, z). Each Fourier mode $\boldsymbol{u}_{\boldsymbol{k}}$ corresponding to the wavevector $\boldsymbol{k} = (k_x, k_y, k_z)$ evolves according to

$$\frac{\mathrm{d}\boldsymbol{u}_{\boldsymbol{k}}}{\mathrm{d}\tau} = \left[\boldsymbol{U}^{2D} \times \boldsymbol{\omega} + \boldsymbol{u} \times \boldsymbol{\Omega}^{2D}\right]_{\boldsymbol{k}} + \mathrm{i}k_z \left(1 - \frac{1}{S^3}\right)\left[W^{2D}\boldsymbol{u}\right]_{\boldsymbol{k}} \\ -\mathrm{i}\boldsymbol{k}\left[p + \boldsymbol{U}^{2D} \cdot \boldsymbol{u}\right]_{\boldsymbol{k}} - \frac{1}{Re}\left(k_x^2 + k_y^2 + \frac{k_z^2}{S^3}\right)\boldsymbol{u}_{\boldsymbol{k}}, \tag{4.13}$$

where $[\cdot]_{\boldsymbol{k}}$ denotes the $\boldsymbol{k}$-Fourier coefficient of the term inside the brackets. Note that relation $\partial_z W^{2D} = 0$ is used to derive equation (4.13). Following standard practice, each Fourier mode $\boldsymbol{u}_{\boldsymbol{k}}$ is then decomposed into a component $\boldsymbol{u}_{\boldsymbol{k}}^{\parallel}$ parallel to the wavevector $\boldsymbol{k}$ and a component $\boldsymbol{u}_{\boldsymbol{k}}^{\perp}$ orthogonal to it. The temporal evolution of $\boldsymbol{u}_{\boldsymbol{k}}^{\perp}$ is obtained by projecting equation (4.13) onto the plane orthogonal to $\boldsymbol{k}$:

$$\frac{\mathrm{d}\boldsymbol{u}_{\boldsymbol{k}}^{\perp}}{\mathrm{d}\tau} = \mathsf{P}_{\boldsymbol{k}}^{\perp}\left(\left[\boldsymbol{U}^{2D} \times \boldsymbol{\omega} + \boldsymbol{u} \times \boldsymbol{\Omega}^{2D}\right]_{\boldsymbol{k}} + \mathrm{i}k_z\left(1 - \frac{1}{S^3}\right)\left[W^{2D}\boldsymbol{u}\right]_{\boldsymbol{k}}\right) \\ -\frac{1}{Re}\left(k_x^2 + k_y^2 + \frac{k_z^2}{S^3}\right)\boldsymbol{u}_{\boldsymbol{k}}^{\perp}, \tag{4.14}$$

where the symbol $\mathsf{P}_{\boldsymbol{k}}^{\perp}$ stands for the projection operator. The parallel component $\boldsymbol{u}_{\boldsymbol{k}}^{\parallel}$ is thereafter obtained as a by-product of the modified incompressibility condition (4.4) as explained below. The usual divergence-free condition $\boldsymbol{k} \cdot \boldsymbol{u}_{\boldsymbol{k}} = 0$ would impose $\boldsymbol{u}_{\boldsymbol{k}}^{\parallel} = 0$. The modified condition (4.4) now yields

$$\boldsymbol{k} \cdot \boldsymbol{u}_{\boldsymbol{k}} = \left(1 - \frac{1}{S^3}\right) k_z u_{z,\boldsymbol{k}}\ , \tag{4.15}$$

where $u_{z,\boldsymbol{k}}$ denotes the axial component of $\boldsymbol{u}_{\boldsymbol{k}}$. As a consequence, the following relation between $\boldsymbol{u}_{\boldsymbol{k}}^{\perp}$ and $\boldsymbol{u}_{\boldsymbol{k}}$ is established:

$$\boldsymbol{u}_{\boldsymbol{k}}^{\perp} \equiv \mathsf{P}_{\boldsymbol{k}}^{\perp}\boldsymbol{u}_{\boldsymbol{k}} \equiv \boldsymbol{u}_{\boldsymbol{k}} - \frac{\boldsymbol{k} \cdot \boldsymbol{u}_{\boldsymbol{k}}}{\boldsymbol{k}^2}\boldsymbol{k} = \boldsymbol{u}_{\boldsymbol{k}} - \left(1 - \frac{1}{S^3}\right)\frac{k_z u_{z,\boldsymbol{k}}}{\boldsymbol{k}^2}\boldsymbol{k}. \tag{4.16}$$

This relation may be easily inverted to yield the three components of $\boldsymbol{u}_{\boldsymbol{k}}$ from the components $(u_{x,\boldsymbol{k}}^{\perp}, u_{y,\boldsymbol{k}}^{\perp}, u_{z,\boldsymbol{k}}^{\perp})$ of $\boldsymbol{u}_{\boldsymbol{k}}^{\perp}$:

$$u_{x,\boldsymbol{k}} = u_{x,\boldsymbol{k}}^{\perp} + \left(1 - \frac{1}{S^3}\right)\frac{k_x k_z}{\boldsymbol{k}^2}\left[1 - \frac{k_z^2}{\boldsymbol{k}^2}\left(1 - \frac{1}{S^3}\right)\right]^{-1} u_{z,\boldsymbol{k}}^{\perp}, \tag{4.17}$$

$$u_{y,\boldsymbol{k}} = u^{\perp}_{y,\boldsymbol{k}} + \left(1 - \frac{1}{S^3}\right) \frac{k_y k_z}{\boldsymbol{k}^2} \left[1 - \frac{k_z^2}{\boldsymbol{k}^2}\left(1 - \frac{1}{S^3}\right)\right]^{-1} u^{\perp}_{z,\boldsymbol{k}}, \tag{4.18}$$

$$u_{z,\boldsymbol{k}} = \left[1 - \frac{k_z^2}{\boldsymbol{k}^2}\left(1 - \frac{1}{S^3}\right)\right]^{-1} u^{\perp}_{z,\boldsymbol{k}}. \tag{4.19}$$

Let $\delta\tau$ denote the time step. The velocity perturbation $\boldsymbol{u}(\tau + \delta\tau)$ is computed using $\boldsymbol{u}(\tau)$ and $\boldsymbol{u}(\tau - \delta\tau)$ as follows. The application of a fast Fourier transform first provides $\boldsymbol{u}_{\boldsymbol{k}}(\tau)$ from which $u^{\perp}_{x,\boldsymbol{k}}(\tau)$, $u^{\perp}_{y,\boldsymbol{k}}(\tau)$ and $u^{\perp}_{z,\boldsymbol{k}}(\tau)$ are extracted using (4.16). The time advance is then performed by discretizing equation (4.14) according to an explicit second-order Adams–Bashforth scheme:

$$\boldsymbol{u}^{\perp}_{\boldsymbol{k}}(\tau + \delta\tau) = e\boldsymbol{u}^{\perp}_{\boldsymbol{k}}(\tau) + \left[\tfrac{3}{2} e \boldsymbol{P}^{\perp}_{\boldsymbol{k}}(\tau) - \tfrac{1}{2} e^2 \boldsymbol{P}^{\perp}_{\boldsymbol{k}}(\tau - \delta\tau)\right] \delta\tau, \tag{4.20}$$

where the damping factor $e = \exp\{-(k_x^2 + k_y^2 + S^{-3}k_z^2)\delta\tau/Re\}$ stems from the exact integration of the modified viscous term. Vector $\boldsymbol{P}^{\perp}_{\boldsymbol{k}}(\tau)$ stands for

$$\boldsymbol{P}^{\perp}_{\boldsymbol{k}}(\tau) = \boldsymbol{P}^{\perp}_{\boldsymbol{k}} \left(\left[\boldsymbol{U}^{2\mathrm{D}} \times \boldsymbol{\omega} + \boldsymbol{u} \times \boldsymbol{\Omega}^{2\mathrm{D}}\right]_{\boldsymbol{k}} + \mathrm{i}k_z \left(1 - \frac{1}{S^3}\right) \left[W^{2\mathrm{D}}\boldsymbol{u}\right]_{\boldsymbol{k}} \right) \tag{4.21}$$

evaluated at time τ. Note that products $\boldsymbol{U}^{2\mathrm{D}} \times \boldsymbol{\omega} + \boldsymbol{u} \times \boldsymbol{\Omega}^{2\mathrm{D}}$ and $W^{2\mathrm{D}}\boldsymbol{u}$ are first evaluated in physical space, then transformed in spectral space and finally projected onto the plane perpendicular to $\boldsymbol{k}$. The above procedure yields the three components $u^{\perp}_{x,\boldsymbol{k}}(\tau+\delta\tau)$, $u^{\perp}_{y,\boldsymbol{k}}(\tau+\delta\tau)$ and $u^{\perp}_{z,\boldsymbol{k}}(\tau+\delta\tau)$. It can be checked that the property $\boldsymbol{u}^{\perp}_{\boldsymbol{k}} \cdot \boldsymbol{k} = 0$, by construction of vector $\boldsymbol{P}^{\perp}_{\boldsymbol{k}}(\tau)$, is verified at $\tau + \delta\tau$ by simply taking the dot product of equation (4.20) with $\boldsymbol{k}$. Relations (4.17)–(4.19) then provide $\boldsymbol{u}_{\boldsymbol{k}}(\tau + \delta\tau)$ and eventually lead to $\boldsymbol{u}(\tau + \delta\tau)$ via a reverse Fourier transform.

In this numerical Fourier formulation, periodic boundary conditions are enforced and the computational domain consists of a cubic box of size $L = 10.24$, meshed by a Cartesian grid of 128^3 collocation points with spacing $\delta l = 0.08$ in the three directions. Along the x- and y-axes, the computational domain is wide enough relative to the vortex diameter that the numerical solution satisfactorily approximates the dynamics of an isolated vortex in an infinite medium. Along the vortex z-axis, periodicity imposes a discretization in the axial wavenumber spectrum: the maximum wavenumber equals $\pi/\delta l \approx 40$ and successive axial wavenumbers are separated by $\delta k_z = 2\pi/L \approx 0.61$. One may wonder whether this numerical spacing of axial wavenumber δk_z is small enough. First, note that the time evolution of each axial mode computed is properly taken into account, since the equations are linear and homogeneous in the z-direction. Second, figure 2 indicates that for any given azimuthal number, the region where the stability curve reaches its maximum contains at least one discretized wavenumber. As a consequence, it is expected that this spacing δk_z is sufficient to get the main part of the phenomenology, in particular the correct time evolution and spatial structures. This feature has been checked by performing a simulation in which the k_z spacing is reduced by a factor two. This is done by doubling the streamwise extent L_z. No major consequences have been detected. In order to satisfy a CFL-type condition, the time step $\delta\tau$ is chosen in the range $1 - 5 \times 10^{-3}$. During the simulation, the time step $\delta\tau$ is adapted – especially during a vortex compression phase, since the time t diverges when the dimensionless time τ approaches $W_0/(a_0\gamma_0)$ (see equation (2.14)).

5. Results

Instability for an unsteady basic flow such as (2.8)–(2.9) is not as straightforward a notion as for a steady state. For a steady basic flow, the instability criterion is defined through a norm based, for instance, on the kinetic energy of the perturbations

$$I(t) = \int_{\mathscr{V}} (u^2 + v^2 + w^2) r \mathrm{d}r \mathrm{d}\theta \mathrm{d}z \tag{5.1}$$

over some physical domain $\mathscr{V}$ (hereafter the computational domain). The equivalent quantity I^0 for the basic flow is constant. When the flow is unsteady, one cannot quantify how perturbations modify the flow structure as time evolves simply by using $I(t)$ since the basic state and therefore I^0 are time dependent. In such a case, ratios between perturbation and basic-state energies seem more appropriate. For instance, one may examine the two ratios $I_{\mathrm{pl}}(t)/I^0_{\mathrm{pl}}(t)$, $I_{\mathrm{ax}}(t)/I^0_{\mathrm{ax}}(t)$ where

$$\left.\begin{aligned} I_{\mathrm{pl}}(t) &= \int_{\mathscr{V}} (u^2 + v^2) r \mathrm{d}r \mathrm{d}\theta \mathrm{d}z, & I^0_{\mathrm{pl}}(t) &= \int_{\mathscr{V}} U_\theta^2 r \mathrm{d}r \mathrm{d}\theta \mathrm{d}z, \\ I_{\mathrm{ax}}(t) &= \int_{\mathscr{V}} w^2 r \mathrm{d}r \mathrm{d}\theta \mathrm{d}z, & I^0_{\mathrm{ax}}(t) &= \int_{\mathscr{V}} W^2 r \mathrm{d}r \mathrm{d}\theta \mathrm{d}z. \end{aligned}\right\} \tag{5.2}$$

Note that only the vortical part, and not the external strain, is used to compute the basic flow energy. Similar quantities may be defined in the transformed system:

$$\left.\begin{aligned} J_{\mathrm{pl}}(t) &= \int_{\mathscr{V}} (\bar{u}^2 + \bar{v}^2) \bar{r} \mathrm{d}\bar{r} \mathrm{d}\theta \mathrm{d}\bar{z}, & J^0_{\mathrm{pl}}(t) &= \int_{\mathscr{V}} (U_\theta^{2\mathrm{D}})^2 \bar{r} \mathrm{d}\bar{r} \mathrm{d}\theta \mathrm{d}\bar{z}, \\ J_{\mathrm{ax}}(t) &= \int_{\mathscr{V}} \bar{w}^2 \bar{r} \mathrm{d}\bar{r} \mathrm{d}\theta \mathrm{d}\bar{z}, & J^0_{\mathrm{ax}}(t) &= \int_{\mathscr{V}} (W^{2\mathrm{D}})^2 \bar{r} \mathrm{d}\bar{r} \mathrm{d}\theta \mathrm{d}\bar{z}. \end{aligned}\right\} \tag{5.3}$$

It is noteworthy that the following equalities hold between the ratios written in the original and transformed systems:

$$\frac{J_{\mathrm{pl}}(t)}{J^0_{\mathrm{pl}}(t)} = \frac{I_{\mathrm{pl}}(t)}{I^0_{\mathrm{pl}}(t)}, \quad \frac{J_{\mathrm{ax}}(t)}{J^0_{\mathrm{ax}}(t)} = \frac{I_{\mathrm{ax}}(t)}{I^0_{\mathrm{ax}}(t)}. \tag{5.4}$$

In the present study, J^0_{pl} and J^0_{ax} are constant since the action of viscous diffusion on the basic flow $\boldsymbol{U}^{2\mathrm{D}}$ is neglected. As a consequence, the study of ratios (5.4) amounts, in this unsteady case, to examining the evolution of $J_{\mathrm{pl}}(t)$ and $J_{\mathrm{ax}}(t)$ in a fashion very similar to that used for steady flows. In what follows the ratios written in the original and transformed systems are used indiscriminantly. Some insight into the flow axial structure may be also obtained by examining two functions of the axial variable $\bar{z}$:

$$j_{\mathrm{pl}}(\bar{z}, \tau) = \int (\bar{u}^2 + \bar{v}^2) \bar{r} \mathrm{d}\bar{r} \mathrm{d}\theta, \qquad j_{\mathrm{ax}}(\bar{z}, \tau) = \int \bar{w}^2 \bar{r} \mathrm{d}\bar{r} \mathrm{d}\theta, \tag{5.5}$$

which denote the instantaneous energy, at the streamwise location $\bar{z}$, of transverse and axial velocities respectively.

In the following, the Reynolds number is fixed to $Re = 667$ to allow comparison with previous works (Delbende *et al.* 1998). In all the simulations, perturbations are initiated using a random field which is obtained by projecting a spatial white noise on the space of divergence-free fields. At time $t = 0$, this projection is simply performed in Fourier space by applying the operator $\mathsf{P}^{\perp}_{\boldsymbol{k}}$.

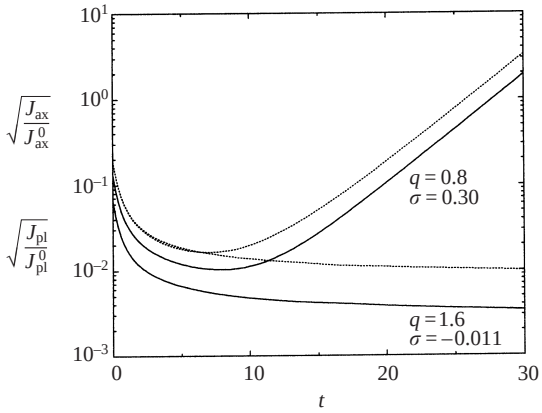

FIGURE 1. Temporal evolution of $(J_{pl}/J^0_{pl})^{1/2}$ (solid line) and $(J_{ax}/J^0_{ax})^{1/2}$ (dotted line) for $\gamma = 0$ at swirl numbers $q = 0.8$ and $q = 1.6$, with $Re = 667$.

5.1. *Simulations with* $\gamma = 0$

The first two simulations are performed with no stretching applied. The usual Batchelor vortex at constant swirl number q is then recovered. Apart from a numerical check, these computations reveal the main features observed when using white noise initial conditions. They hence provide reference cases for later analyses.

Two values of the swirl number $q = 0.8$ and $q = 1.6$ are considered, which correspond to an unstable and a stable configuration respectively (Lessen *et al.* 1974). The Reynolds number is set to $Re = 667$. In figure 1, the temporal evolution of $(J_{pl}/J^0_{pl})^{1/2}$ and $(J_{ax}/J^0_{ax})^{1/2}$ is plotted for both swirl numbers. As expected, the first one displays an asymptotic growth of perturbations, while the second leads to an asymptotic damping.

A transient period of decrease is initially observed corresponding to the damping of most small-scale modes and positive azimuthal wavenumbers. Indeed it is known from classical stability analyses of the Batchelor vortex that azimuthal wavenumbers $n = 0$ and $n \geqslant 2$ are always stable, and mode $n = 1$ is stabilized as soon as $q > 0.074$. The next stage of the simulation is reached when the unstable modes for $q = 0.8$ (respectively the less stable modes for $q = 1.6$) emerge from the initial noise. Note that an instantaneous growth rate can be defined as the amplitude derivative

$$\frac{\mathrm{d}}{\mathrm{d}t}\left[\log\sqrt{\frac{J_{pl}}{J^0_{pl}}}\right]. \tag{5.6}$$

The maximum of this quantity may then be obtained, in the semi-log representation of figure 1, as the asymptotic slope of the plotted curves. For $q = 0.8$, the computed value $\sigma = 0.30$ agrees with the standard stability analyses of the Batchelor vortex.

According to previous studies (Mayer & Powell 1992), the overall maximum inviscid growth of perturbations is attained at $q \approx 0.87$. Moreover, the maximum inviscid growth rate for a fixed swirl number q and negative azimuthal wavenumber n increases with $|n|$ and saturates as $n \to -\infty$ (Leibovich & Stewartson 1982). However, viscosity counterbalances this latter effect thus leading to an overall maximum for a finite value of n. For instance, the growth rate curves $\sigma_n(k_z)$ at $Re = 667$ and swirl number $q = 0.8$ are drawn as solid lines on figure 2 (Delbende *et al.* 1998). The most unstable modes are associated with the azimuthal wavenumber $n = -3$ and axial wavenumber

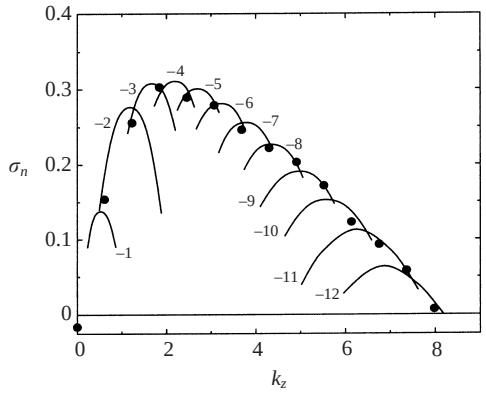

FIGURE 2. Temporal growth rate σ as a function of axial wavenumber k_z for parameters $\gamma = 0$, $q = 0.8$ and $Re = 667$. The symbols ● denote the growth rates of the discrete axial wavenumbers obtained in the present simulation, computed from the time evolution of perturbation spectra. Each solid line (reported from Delbende *et al.* 1998) shows the growth rate $\sigma_n(k_z)$ for each unstable azimuthal wavenumber n (n is indicated near the associated curve) obtained from a viscous DNS-based stability analysis at the same Reynolds number.

$k_z \approx 1.68$ ($\sigma \approx 0.31$), the azimuthal wavenumber $n = -4$ and axial wavenumber $k_z \approx 2.17$ ($\sigma \approx 0.31$) and the azimuthal wavenumber $n = -5$, axial wavenumber $k_z \approx 2.68$ ($\sigma \approx 0.30$). The time evolution of perturbation spectra in the present simulation for $q = 0.8$ may be used to recover, for each discrete axial wavenumber k_z, the associated growth rate σ. More precisely, we have separated, at some given times, the different axial $k_{\bar{z}}$ and azimuthal n wavenumbers of the axial velocity field, which provides various discretized components $u_n(k_{\bar{z}}, r, \tau)$. By integrating this function over r, a quantity is obtained which undergoes an exponential time evolution near the end of the simulation. The growth rate for each $(k_{\bar{z}}, n)$ is then obtained by a primitive two-point interpolation with respect to time. Indeed, this study does not aim at providing an accurate comparison with the theoretical stability results for such modes. These results, plotted as circles in figure 2, are consistent with the growth rate curves $\sigma_n(k_z)$ and indicate that modes emerging in the present simulations must be related to these predominant azimuthal wavenumbers $n = -3$, $n = -4$ and $n = -5$.

5.2. *Simulations with* $\gamma \neq 0$

The third simulation consists of a compression phase immediately followed by a stretching phase. More specifically, the strain rate is set to $\tilde{\gamma} = -0.025$ for $0 \leqslant \tau \leqslant 15$, and to $\tilde{\gamma} = +0.025$ for $15 < \tau \leqslant 30$. Quantity γ is expected to be small when scaled using the vortex characteristics (see e.g. the asymptotic analysis by Moffatt, Kida & Ohkitani 1994). For the same reasons, it is assumed that it fluctuates with a characteristic time larger than the turnover time. Therefore, we choose relatively low values for γ_0 and values significantly larger than 1 for $\tau^\star$. For this strain-rate time evolution, τ (see relations (2.14) and (2.17)) is not identical to physical time t as illustrated in figure 3. The instantaneous swirl number, initially set to $q(0) = 1.8$, decreases during the compression down to the value $q \approx 0.88$, and thereafter increases back towards its initial value (figure 4*a*). Similarly, the basic-state core expands and shrinks back, as depicted in figure 4(*b*). Let us hereafter call the q-region where unstable modes prevail for the unstretched inviscid Batchelor vortex, the Batchelor-vortex instability domain. Initially the basic vortex flow lies outside this region, then penetrates it and finally leaves it. The time evolution of fluctuations perturbing

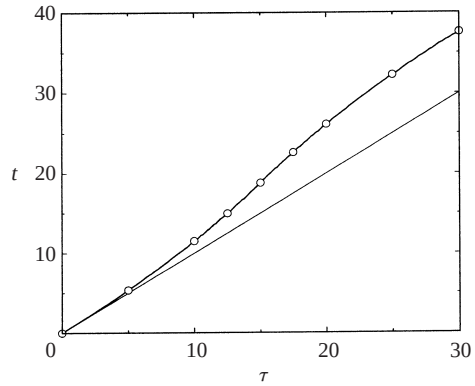

FIGURE 3. Physical time t versus modified time τ used for the simulation with compression and stretching. The circles denote the position of the snapshots pictured in figures 6–10. The straight line indicates function $t = \tau$ prevailing when $\gamma = 0$.

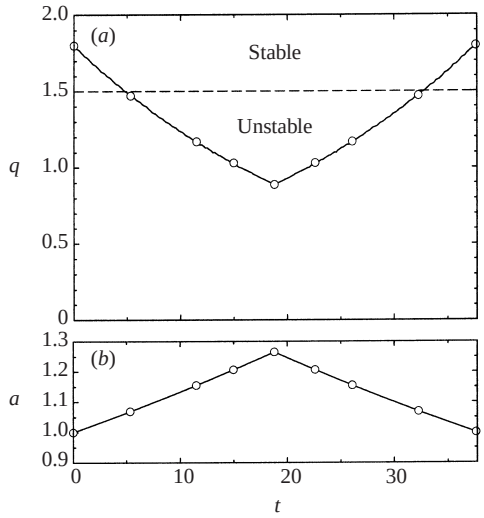

FIGURE 4. Instantaneous (a) swirl number $q(t)$ and (b) core size $a(t)$ as functions of physical time t for the simulation with compression and stretching. The dashed line corresponds to the Batchelor-vortex instability threshold at $q \approx 1.50$. The circles denote the position of the snapshots pictured in figures 6–10.

the above basic flow may be divided as well into three stages (figure 5): an initial energy decrease followed by an instability phase and a re-stabilization. The growth phase lies within the Batchelor-vortex instability domain, though it does not start with the crossing of $q = 1.5$. By contrast, the re-stabilization occurs very close to $q = 1.5$. Within the quasi-static approximation, this latter effect is accounted for in a straightforward manner, since the local dynamics is understood in terms of the stability of an unstretched steady Batchelor vortex with instantaneous swirl number $q(\tau)$. The time delay between growth and penetration into the Batchelor-vortex instability domain is clearly of the same transient nature as the one observed in the unstretched case (figure 1). In other words, these perturbations are not optimal when parameters enter the instability domain. Similar observations were made for other flows, e.g. the Görtler instability (Cossu *et al.* 2000). The instantaneous growth rate

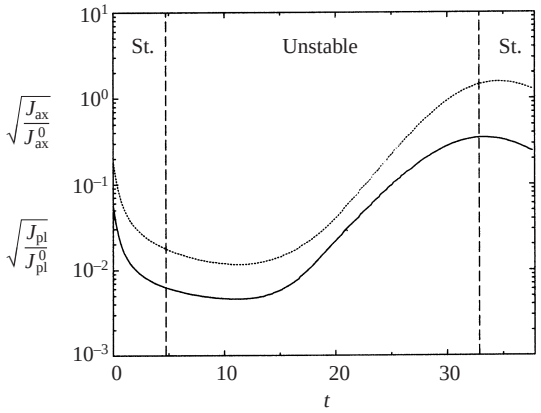

FIGURE 5. Temporal evolution of quantities $(J_{pl}/J_{pl}^0)^{1/2}$ (solid line) and $(J_{ax}/J_{ax}^0)^{1/2}$ (dotted line) for the simulation with compression and stretching. The dashed line corresponds to the Batchelor-vortex instability threshold.

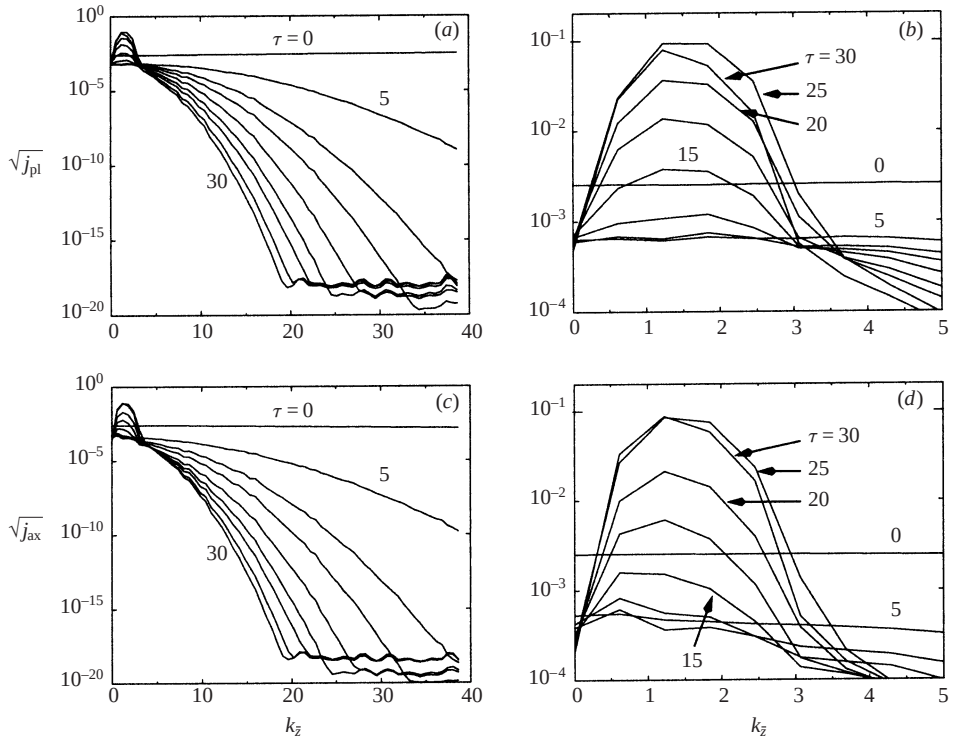

FIGURE 6. Spectrum of transverse $j_{pl}^{1/2}$ (a, b) and axial $j_{ax}^{1/2}$ (c, d) r.m.s. perturbation velocities with respect to the axial wavenumber $k_{\bar{z}}$ at $\tau = 0, 5, 10, 12.5, 15, 17.5, 20, 25, 30$. Frames (b) and (d) are close-ups of the low-wavenumber region, where pertinent phenomena occur.

(5.6) reaches a maximum value 0.35 at $t \approx 20$ (or $\tau \approx 15$), i.e. when $q(\tau) \approx 0.88$. This value may be tentatively compared with the growth rate 0.39 deduced after rescaling the value computed for the unstretched Batchelor vortex of § 5.1 at $q = 0.8$ (see the Appendix for details).

Figure 6 displays at various times τ (corresponding to circles in figures 3 and 4)

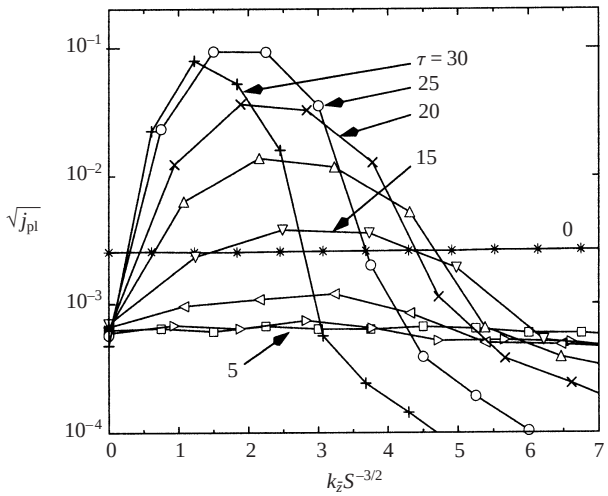

FIGURE 7. Same as figure 6(b) but plotted with respect to the rescaled wavenumber $k_{\bar{z}}S^{-3/2}$.

the spectrum of the instantaneous energies $j_{\rm pl}(\bar{z},\tau)$, $j_{\rm ax}(\bar{z},\tau)$ in terms of the axial wavenumber $k_{\bar{z}}$. At $\tau = 0$, the spectrum is flat, as expected, since white noise is initially introduced. For larger times, a bell-shaped spectrum emerges for both functions at large scales ($k_{\bar{z}} = O(1)$) while small scales are being rapidly damped. Such features ensure that the computational domain is large enough in the axial $\bar{z}$-direction, that the simulation is sufficiently well resolved in spectral space to capture the main flow-instability structures. The quasi-static approximation may provide a qualitative interpretation of such an evolution. Note, however, that, in this latter framework, the reference length scale along the axis is equal to $a_0S^{-3/2}$ (see the end of § 3): $k_{\bar{z}}$, which, in the simulation, is made dimensionless using length scale a_0, must hence be rescaled by a factor $S^{-3/2}$. This rescaling is precisely applied in the companion figure 7. First, the perturbation spectra between $\tau = 10$ and $\tau = 20$ undergo a rapid growth which particularly affects rescaled wavenumbers $k_{\bar{z}}S^{-3/2}$ between 2 and 3. Indeed, the growth rate of an unstretched Batchelor vortex at similar swirl numbers achieves a maximum for axial wavenumbers between 2 and 3 (see figure 2). Secondly, the maximum in figure 7 is progressively shifted, for larger τ, towards smaller rescaled wavenumbers while the interval of amplified wavenumbers is reduced. In this range, the swirl number $q(\tau)$ progressively increases across $q \approx 1.50$: from standard results, it is known that the upper unstable axial wavenumber then decreases while negative helical modes are progressively restabilized, the mode $n = -1$ being the last one to become stable (Delbende *et al.* 1998). This feature explains why, at final time $\tau = 30$, a 'preferred' relatively small axial wavenumber $k_{\bar{z}} \approx 1.25$ emerges through the process of compression and stretching (see curve $\tau = 30$ in figure 7).

The transverse flow structure is represented for different times in figure 8 where isocontours of the axial component of the perturbation vorticity ω_z are plotted at a fixed streamwise location. The physical domain shown is a transverse cut of the vortex centred around its core (the effective computational domain is much larger, which avoids spurious periodic effects). One observes first a filtering of small scales and the gradual appearance of a vortical structure. The observed symmetries indicate the presence of azimuthal wavenumbers $|n| = 4$ and $|n| = 5$ which are reminiscent of the most unstable azimuthal modes of the viscous unstretched Batchelor vortex

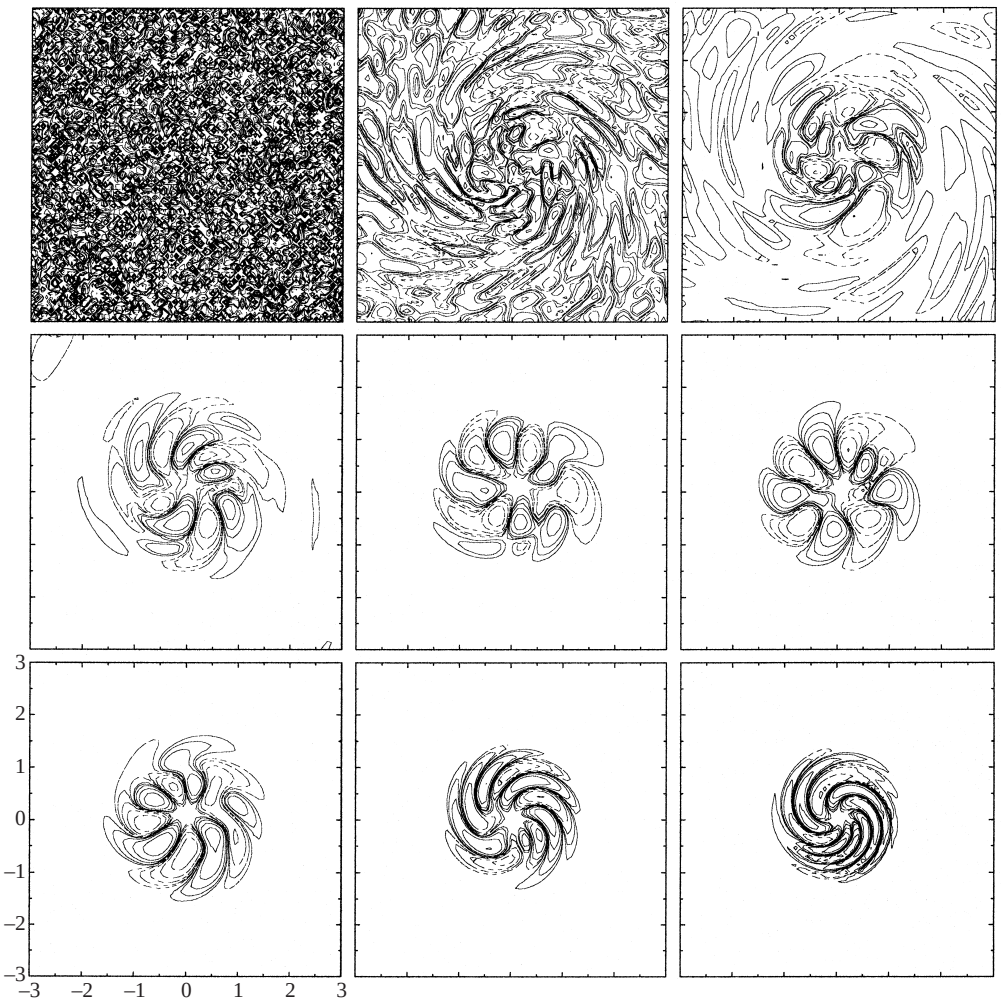

FIGURE 8. Isocontours in the (r, θ)-plane of the axial component ω_z of the perturbation vorticity at a fixed axial location. Contours shown correspond to $\omega_z(r, \theta, t) = \pm\omega_{z,\max}/2^p$, where $p = 1, 2, \cdots, 5$. Positive (resp. negative) values are represented by solid (resp. dashed) lines. Each snapshot corresponds to a circle in figures 3 and 4. Figure should be read from left to right and top to bottom.

at $q = 0.8$. During the subsequent stretching phase, this structure is finally rolled-up. Compression and stretching effects appear on the average vortex core size. A glimpse at the three-dimensional perturbation is given in figure 9 where isosurfaces of the axial vorticity perturbation $\omega_{\bar{z}}$ are shown. Note that the expansion and compression of the vortex core is not apparent here since, unlike in figure 8, the frames are displayed in the modified spatial coordinates in which the vortex core size is constant. These snapshots display the gradual appearance of axial and azimuthal symmetry structures.

The above perturbation structure, when superimposed on the basic unsteady state, leads to the three-dimensional flows displayed in figure 10(a, b). One isosurface of the axial component of the total vorticity field $\Omega_{\bar{z}} = \Omega_{\bar{z}}^{2D} + \omega_{\bar{z}}$ is presented for two different initial r.m.s. perturbation levels $(J_{\rm pl}(0)/J_{\rm pl}^0)^{1/2} = 8 \times 10^{-4}$ for figure 10(a) and

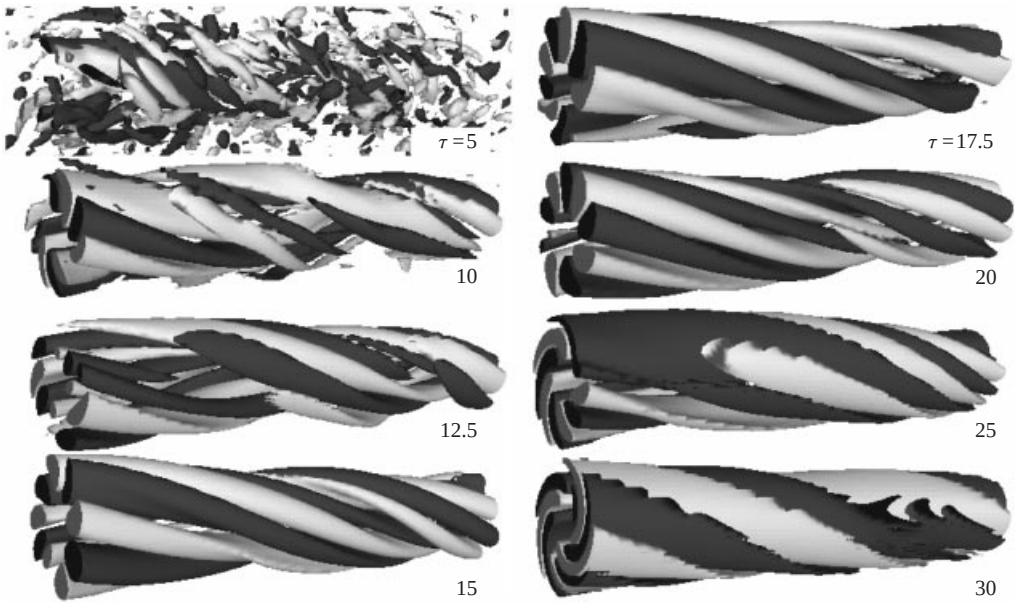

FIGURE 9. Isosurfaces of the axial component $\omega_{\bar{z}}$ of the perturbation vorticity for $\omega_{\bar{z}}(\bar{r},\theta,\bar{z},\tau) = \pm\frac{1}{2}\omega_{\bar{z},\max}$. Each snapshot corresponds to a circle in figures 3 and 4. Note that the conical aspect of the vortex is only due to the geometrical perspective.

$(J_{\rm pl}(0)/J^0_{\rm pl})^{1/2} = 1.4\times10^{-2}$ for figure 10(*b*). Results are shown until the maximum of perturbation $\omega_{\bar{z}}(\tau)$ becomes larger than the maximum of the basic flow $\Omega^{\rm 2D}_{\bar{z}}$. When both amplitudes are of the same order of magnitude, this procedure is pertinent only if nonlinear terms mainly affect the amplitude without drastically modifying the spatial perturbation structure selected through the linear evolution. This hypothesis, known to be valid in the framework of weakly nonlinear analyses, is an attempt to reveal the nonlinear structure that may emerge from the compression and stretching process. Such an assumption remains to be verified using a fully nonlinear simulation code, which is outside the scope of the present paper. These frames indicate that the vortex becomes corrugated as in a Matisse collage (Matisse 1952) with 4 or 5 lobes. It is conjectured that a further evolution into the nonlinear regime might lead to the formation of several interwoven filaments as observed in the experiment by Cadot, Douady & Couder (1995) and in the numerical simulation of the nonlinear evolution of the unstretched Batchelor vortex by Delbende & Chomaz (2000).

The influence of the time $T_{\rm inst}$ spent by the perturbation within the Batchelor-vortex instability domain is now investigated. Figure 11(*a*, *b*) shows the results of various simulations of compression and stretching processes with $\tilde{\gamma} = \pm0.05$ for various time intervals $T_{\rm inst}$ (see figure 11*a*). The initial swirl $q(0)$ is now set to the value 1.6. The total amplification gain† which results from the excursion of the perturbation inside the Batchelor-vortex instability domain can be deduced from the energy curves on figure 11(*b*). It clearly increases with the time interval $T_{\rm inst}$ as expected from a naive quasi-static approximation. On curve (i), the vortex remains inside the instability

† It is clear, as for any linear evolution, that the displayed total gains computed over a finite time depend on the selected initial conditions. The present curves are obtained for an initial divergence-free white noise field. Larger amplitudes could certainly be reached with more optimal initial conditions.

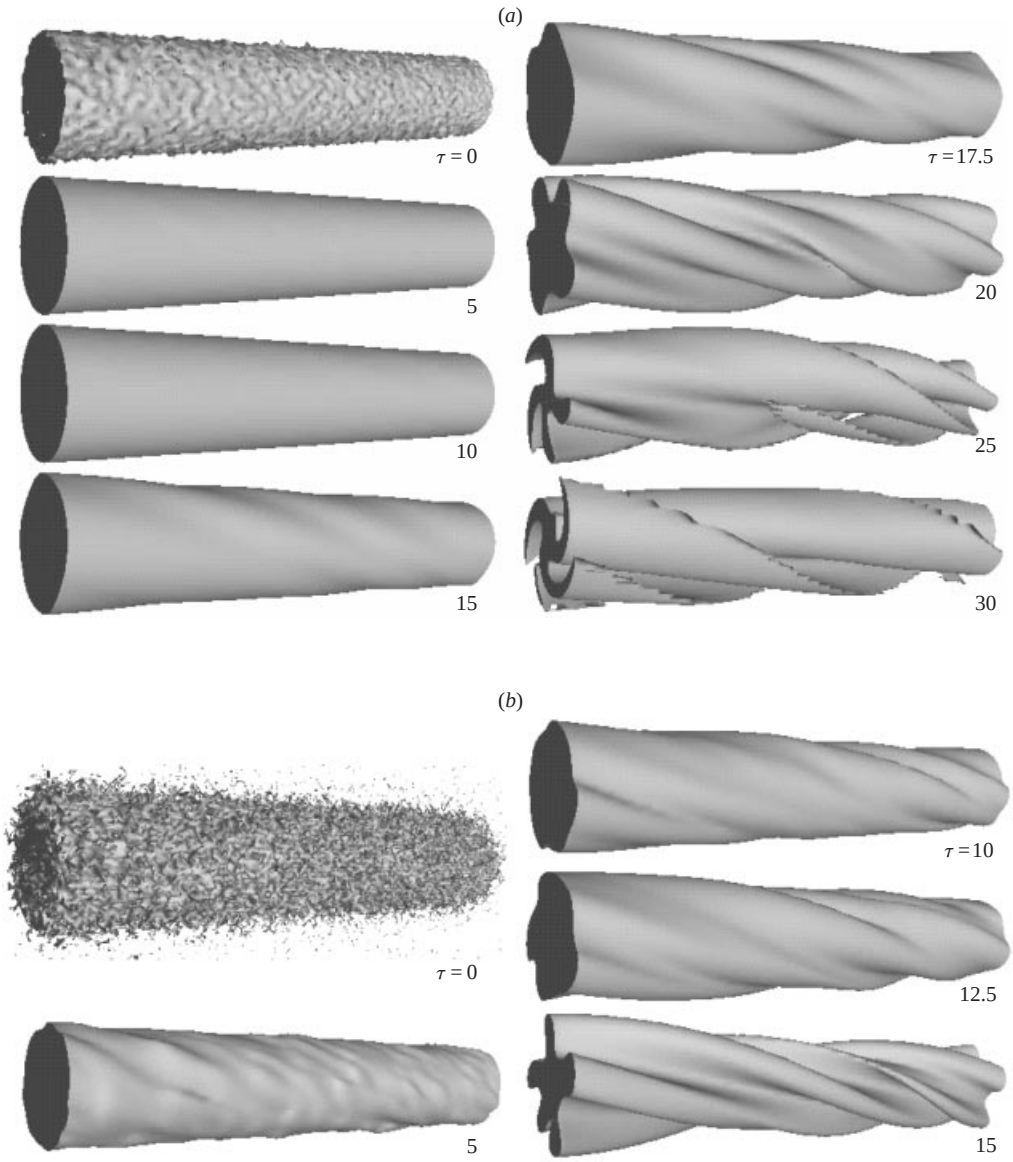

FIGURE 10. Isosurfaces of the axial component $\Omega_{\bar{z}}$ of the total vorticity for $\Omega_{\bar{z}}(\bar{r}, \theta, \bar{z}, \tau) = \frac{1}{2}\Omega_{\bar{z},\max}$. For series ($a$), the simulation is initiated with a r.m.s. value $(J_{\rm pl}(0)/J^0_{\rm pl})^{1/2} = 8 \times 10^{-4}$. For series ($b$), a stronger noise amplitude is used $(J_{\rm pl}(0)/J^0_{\rm pl})^{1/2} = 1.4 \times 10^{-2}$. Each snapshot corresponds to a circle in figures 3 and 4. Note that the conical aspect of the vortex is only due to the geometrical perspective.

region for a short period, and energy is always decreasing. On curve (ii), the total amplification is less than unity even though the energy temporarily increases. By contrast, curves (iii) and (iv) are characterized by respective substantial gains of order 10 and 100. Note that on curve (iv), the amplitude derivative (5.6) has a local minimum (near $t = 22$) inside the Batchelor-vortex instability domain. This feature may be revealed by the quasi-static approximation since the instantaneous growth rate of an associated unstretched Batchelor vortex following the path $q(t)$ on figure 11(a),

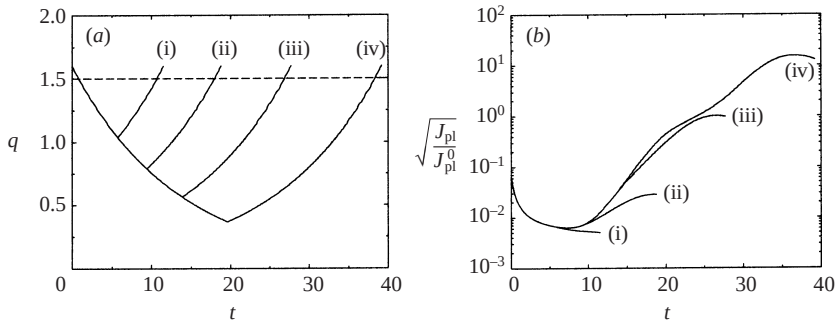

FIGURE 11. Various simulations (i–iv) with compression and stretching for the same value of $\tilde{\gamma} = \pm 0.05$ and for various time intervals T_{inst}. (a) Instantaneous swirl number $q(t)$; (b) temporal evolution of energy $(J_{\text{pl}}/J_{\text{pl}}^0)^{1/2}$.

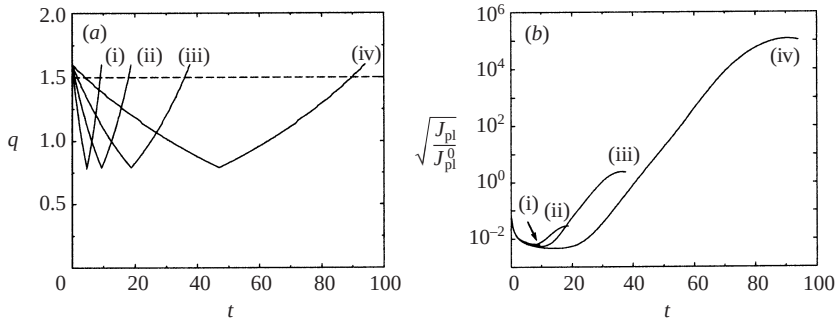

FIGURE 12. Various simulations (i–iv) with compression and stretching for different values of $\tilde{\gamma}$ (respectively ± 0.1, ± 0.05, ± 0.025, ± 0.01). (a) Instantaneous swirl number $q(t)$; (b) temporal evolution of energy $(J_{\text{pl}}/J_{\text{pl}}^0)^{1/2}$.

reaches a local minimum at $t \approx 20$. In the same spirit, figure 12(a) presents various simulations performed with the same $q(t_\star) \approx 0.8$ (i.e. swirl numbers cross the same instability region) but with different γ values. In that case, the time spent T_{inst} is also changed. Once $|\gamma|$ increases, the time spent in the instability region decreases until the amplification mechanism is no longer active (in figure 12 when $|\tilde{\gamma}| > 0.05$).

In turbulent flows, vortex filaments are subjected to fluctuating strain caused by large-scale structures. The simple process defined by figures 11 and 12 aims at emulating such fluctuations and provides the following mechanism: a stable vortex is first brought inside the Batchelor-vortex instability domain by a sufficiently long compression. It remains in that region and grows until γ, which expresses the action of surrounding large scales, changes sign. Stretching then makes the vortex leave the instability domain, which stops the perturbation growth. If perturbations have reached a high enough amplitude, the vortex may be disrupted because of nonlinear interactions. This two-step mechanism tentatively explains the abrupt destruction of vortices as observed in turbulent flows.

6. Conclusion

In this paper, the three-dimensional linear stability problem of a stretched vortex with axial flow has been addressed. It has first been shown that these stability equations could be reduced to equations similar to those governing perturbations of

an unstretched vortex, however with particular time-varying parameters. It has also been argued how this slight difference (an additionnal time-varying factor in the axial derivatives) drops out in a quasi-static approximation. This regime should be valid in the limit of weak stretching and large Reynolds numbers.

The general perturbation equations for the stretched Batchelor vortex have then been numerically solved for particular variations of the stretching rate, using white noise as initial condition. Compressing and stretching the vortex leads to the appearance of axial and azimuthal symmetry structures whereby the vortex becomes corrugated with several lobe structures. In addition, the local time evolution of perturbations may be understood in the framework of a quasi-static approximation provided the strain rate is not too large.

Results were also discussed in the context of turbulence. The stretched Batchelor vortex subjected to the prototype stretching field might mimic the behaviour of filaments in a turbulent background flow and their destruction could be due to the modification of the vortex characteristics by stretching. This mechanism is clearly different from the elliptic instability mechanism (Le Dizès *et al.* 1996; Eloy & Le Dizès 1999) although both could be active in turbulence. In the elliptical mechanism, the instability is generated by the stretching field and not by the vortex itself. In particular, the local growth rate of the elliptical instability is proportional to the non-axisymmetric component of the stretching rate and therefore it is expected to be much smaller than the growth rate of the Batchelor vortex instability, which is proportional to the axial vorticity of the vortex.

The nonlinear interactions which are needed to describe the vortex destruction have not been considered in the present analysis. This constitutes an important issue as nonlinear effects can induce both rich dynamics in the Batchelor vortex (Abid & Brachet 1998; Delbende & Chomaz 2000) and strong modification of the stretching field (Abid *et al.* 2002). Linear aspects are also not fully explored as we have not tried to seek the most unstable perturbation. The determination of the optimal perturbation is indeed an open issue which could have important applications in aeronautics. In the context of vortex stability, such an issue has only been addressed by Nolan & Farrell (1999) for two-dimensional perturbations in a class of tornado-like vortices. In future work, it would be interesting to extend their analysis to the three-dimensional problem and to perform a full generalized three-dimensional stability analysis (Farrell & Ioannou 1996) of the system (3.20)–(3.23).

We would like to acknowledge the use of a NEC–SX5 supercomputer at IDRIS–CNRS in the frame of projects CP2–#990173 and #000173. Thanks to Dang Anh-Tuân for his rapid and kind technical assistance.

Appendix

In the framework of the quasi-static approximation, the instantaneous growth rate (5.6) at time t is associated with the growth rate of an unstretched Batchelor vortex at $q(\tau)$ provided that a proper normalization factor is taken into account. This latter quantity arises because the unstretched vortex dimensionless characteristics are evaluated (i) using time τ and (ii) with the time scale $a(t)/W(t) = S(\tau)^{1/2}a_0/W_0$. This implies that the standard growth rate must be divided by a factor $S(\tau)$ to account for the relation $\mathrm{d}\tau = s(t)\mathrm{d}t$ and multiplied by a factor $S(\tau)^{1/2}$ since the time scale of the simulation is taken to be a_0/W_0.

In the simulation considered in § 5.2, the instantaneous growth rate 0.35 is obtained

at $t \approx 20$ (or $\tau \approx 15$) and may be associated with the the standard growth rate 0.31 (computed for the unstretched Batchelor vortex at $q = 0.8$ in § 5.1) which, divided by an overall factor $S(\tau = 15)^{1/2} \approx 0.79$, yields 0.39. Note, however, that this is only a rough estimate since the swirl number 0.8 used for comparison purposes is located slightly below the lower value for $q(\tau)$ and since the Reynolds number should also be rescaled.

REFERENCES

Abid, M., Andreotti, B., Douady, S. & Nore, C. 2002 Oscillating structures in a stretched-compressed vortex. *J. Fluid Mech.* **450**, 207–233.

Abid, M. & Brachet, M. E. 1998 Direct numerical simulations of the Batchelor trailing vortex by a spectral method. *Phys. Fluids* **10**, 469–475.

Andreotti, B., Douady, S. & Couder, Y. 1997 About the interaction between vorticity and stretching. In *Turbulence Modelling and Vortex Dynamics* (ed. O. Boratav, A. Eden & A. Erzan). Lecture Notes in Physics, pp. 92–107. Springer.

Ash, R. L. & Khorrami, M. R. 1995 Vortex stability. In *Fluid Vortices* (ed. Green, S. I.), Chap VIII, pp. 317–372. Kluwer.

Batchelor, G. K. 1964 Axial flow in trailing line vortices. *J. Fluid Mech.* **20**, 645–658.

Batchelor, G. K. & Proudman, I. 1954 The effect of rapid distortion in a fluid in turbulent motion. *Q. J. Mech. Appl. Maths* **7**, 83–103.

Cadot, O., Douady, S. & Couder, Y. 1995 Characterization of the low pressure filaments in three-dimensional turbulent shear flow. *Phys. Fluids* **7**, 630–646.

Cambon, C. & Scott, J. F. 1999 Linear and nonlinear models of anisotrop turbulence. *Annu. Rev. Fluid Mech.* **31**, 1–53.

Cossu, C., Chomaz, J.-M., Huerre, P. & Costa, M. 2000 Maximum spatial growth of Görtler vortices. *Flow, Turbul. Combust.* **65**, 369–392.

Craik, A. D. D. & Criminale, W. O. 1986 Evolution of wavelike disturbances in shear flows: a class of exact solutions of the Navier-Stokes equations. *Proc. R. Soc. Lond.* A **406**, 13–26.

Delbende, I. & Chomaz, J.-M. 2000 Bursting of a swirling jet stemming from a localized perturbation. In *Vortex Structure and Dynamics* (ed. A. Maurel & P. Petitjeans). Lecture Notes in Physics, pp. 140–146. Springer.

Delbende, I., Chomaz, J.-M. & Huerre, P. 1998 Absolute/convective instabilities in the Batchelor vortex: a numerical study of the linear impulse response. *J. Fluid Mech.* **355**, 229–254.

Eloy, C. & Le Dizès, S. 1999 Three-dimensional instability of Burgers and Lamb-Oseen vortices in a strain field. *J. Fluid Mech.* **378**, 145–166.

Escudier, M. P. 1988 Vortex breakdown: observations and explanations. *Prog. Aerospace Sci.* **25**, 189–229.

Farrell, B. F. & Ioannou, P. J. 1996 Generalized stability theory. Part I: Autonomous Operators. Part II: Nonautonomous operators. *J. Atmos. Sci.* **53**, 2025–2053.

Gibbon, J. D., Fokas, A. S. & Doering, C. R. 1999 Dynamically stretched vortices as solution of the 3D Navier–Stokes equations. *Physica* D **132**, 497–510.

Le Dizès, S., Rossi, M. & Moffatt, H. K. 1996 On the three-dimensional instability of elliptical vortex subjected to stretching. *Phys. Fluids* **8**, 2084–2090.

Leibovich, S. 1978 The structure of vortex breakdown. *Annu. Rev. Fluid Mech.* **10**, 221–246.

Leibovich, S. 1983 Vortex stability and breakdown: survey and extension. *AIAA J.* **17**, 471–477.

Leibovich, S. & Stewartson, K. 1983 A sufficient condition for the instability of columnar vortices. *J. Fluid Mech.* **126**, 335–356.

Lessen, M. & Paillet, F. 1974 The stability of a trailing line vortex. Part 2. Viscous theory. *J. Fluid Mech.* **65**, 769–779.

Lessen, M., Singh, P.J. & Paillet, P. 1974 The stability of a trailing line vortex. Part 1. Inviscid theory. *J. Fluid Mech.* **63**, 753–763.

Lundgren, T. S. 1982 Strained spiral vortex model for turbulent fine structure. *Phys. Fluids* **25**, 2193–2203.

Marshall, J. S. 1997 The flow induced by periodic vortex rings wrapped around a columnar vortex core. *J. Fluid Mech.* **345**, 1–30.

Matisse, H. 1952 *La Tristesse du Roi*. Musée National d'Art Moderne, Paris.

Maurel, A. & Petitjeans, P. (Eds.) 2000 *Vortex Structure and Dynamics*. Springer.

Mayer, E. W. & Powell, K. G. 1992 Viscous and inviscid instabilities of a trailing line vortex. *J. Fluid Mech.* **245**, 91–114.

Moffatt, H. K., Kida, S. & Ohkitani, K. 1994 Stretched vortices – the sinews of turbulence; large-Reynolds-number asymptotics. *J. Fluid Mech.* **259**, 241–264.

Nolan, D. S. & Farrell, B. F. 1999 Generalized stability analyses of asymmetric disturbances in one- and two-celled vortices maintained by radial inflow. *J. Atmos. Sci.* **56**, 1282–1307.

Olendraru, C., Sellier, A., Rossi, M. & Huerre, P. 1996 Absolute/convective instability of the Batchelor vortex. *C. R. Acad. Sci. Paris* **323**, 153–159.

Olendraru, C., Sellier, A., Rossi, M. & Huerre, P. 1999 Inviscid instability of the Batchelor vortex: Absolute/convective transition and spatial branches. *Phys. Fluids* **11**, 1805–1820.

Petitjeans, P., Robres, J. H., Wesfreid, J. E. & Kevlahan, N. 1998 Experimental evidence for a new type of stretched vortices. *Eur. J Mech.*B/*Fluids* **17**, 549–560.

Pullin, D. I. & Saffman, P. G. 1998 Vortex dynamics in turbulence. *Ann. Rev. Fluid Mech.* **30**, 31–51.

Rossi, M. 2000 Of vortices and vortical layers: an overview. In *Vortex Structure and Dynamics* (ed. A. Maurel & P. Petitjeans). Lecture Notes in Physics, pp. 40–123. Springer.

Rossi, M. & Le Dizès, S. 1997 Three-dimensional stability spectrum of stretched vortices. *Phys. Rev. Lett.* **78**, 2567–2569.

Verzicco, R. & Jiménez, J. 1999 On the survival of strong vortex filaments in 'model' turbulence. *J. Fluid Mech.* **394**, 261–279.

Verzicco, R., Jiménez, J. & Orlandi, P. 1995 On steady columnar vortices under local compression. *J. Fluid Mech.* **299**, 367–388.

Vincent, A. & Meneguzzi, M. 1991 The spatial structure and statistical properties of homogeneous turbulence. *J. Fluid Mech.* **225**, 1–20.